Bulletin of the Seismological Society of America, Vol. 101, No. 4, pp. 1554–1562, August 2011, doi: 10.1785/0120100186

Seismic Investigation of the 26 March 2010 Sinking of the South Korean Naval Vessel *Cheonanham*

by Tae-Kyung Hong

Abstract A South Korean naval vessel sank on 26 March 2010. A seismic event with magnitude (M_L) of 1.5 was observed at the time of vessel-sinking. Seismic waveforms were collected from three local stations. The event origin time is refined based on the *P* and *S* arrival times at the stations. The calculated event location and time are close to the reported vessel-sinking location and time, suggesting that the observed seismic event is associated with the vessel-sinking. The amplitudes of *S* waves are comparable to those of *P* waves. Seismic waves coupled from acoustic waves are observed, providing additional constraints of epicentral distance and source type. The coupled acoustic waves have a dominant frequency of ~32 Hz. The acoustic waves and high P/S amplitude ratios suggest an underwater explosion. The body-wave magnitude based on *Pn* is determined to be 1.46, which is consistent with the reported M_L. *P* energy is dominant at around 8.5 Hz, with multiple frequencies of 17.7 and 34.6 Hz. The primary frequency suggests the water-column thickness in the source region to be 44 m, which agrees with the reported value.

Introduction

A South Korean naval vessel, *Cheonanham*, sank at ~2.5 km southwest of Bakryeong Island (37.929° N, 124.601° E) at 21:22 local time (12:22 UTC) on 26 March 2010 (Multinational Civilian-Military Joint Investigation Group [MCMJIG], 2010). Only 58 people out of the 104 crew members were rescued from the incident, and the other 46 sailors were dead or missing in the incident. Three plausible causes of the sinking were raised: (1) striking by an explosive source (torpedo or mine), (2) shear breakage due to strain accumulation by fatigue, and (3) collision with a sunken rock (MCMJIG, 2010).

Seismic analyses enable me to refine the event origin time and location, and allow me to constrain the source properties such as source type and strength. These features allow me to use the seismic analyses for investigation of incidents (e.g., Ichinose *et al.*, 1999; Kim *et al.*, 2001; Koper *et al.*, 2003; Evers *et al.*, 2007). In particular, underwater explosions can be identified from wave-train composition and spectral features, and their source properties can be investigated using local and regional seismograms (Weinstein, 1968; Plutchok and Broome, 1969; Baumgardt and Der, 1998; Bowers and Selby, 2009).

Seismic record sections at the time of the vessel-sinking were collected from three local stations. I investigate the characteristics of the observed seismograms and infer the source properties.

Events and Data

The South Korean naval vessel sank at a location 2.5 km to the west of Bakryeong Island in the Yellow Sea, located near the border between South Korea and North Korea (Fig. 1, Table 1). The naval vessel had a displacement of 1223 tons, full length of 88.3 m, full breadth of 10 m, and mean draft of 2.88 m (MCMJIG, 2010).

A seismic event with a local magnitude (M_L) of 1.5 was observed at the time of the incident. The event was detected by a local network of the Korea Meteorological Administration (KMA). Three-component velocity waveforms are collected from three permanent stations, BAR, DEI, and GAHB (Fig. 1, Table 2). The sensor types are STS-2 (broadband) for station BAR, CMG-3TB (borehole broadband) for station GAHB, and CMG40T-1 (short-period) for station DEI. The sampling rates are 100 samples per second. Analyses are based on displacement seismograms from which instrument responses were removed. I observe clear arrivals of *P* and *S* waves in seismograms band-pass filtered between 4 and 8 Hz (Fig. 2).

Seismic records of two nearby natural earthquakes are also analyzed for comparison (Fig. 1). The magnitudes of the earthquakes are M_L 3.0 and M_L 2.2, and the focal depths are 8 and 0.6 km (Table 3). I collect seismic records of the same stations (BAR, DEI, GAHB). The seismograms band-pass filtered between 4 and 8 Hz display clear arrivals of *P* and *S* phases (Fig. 3). I find that the seismic records of the

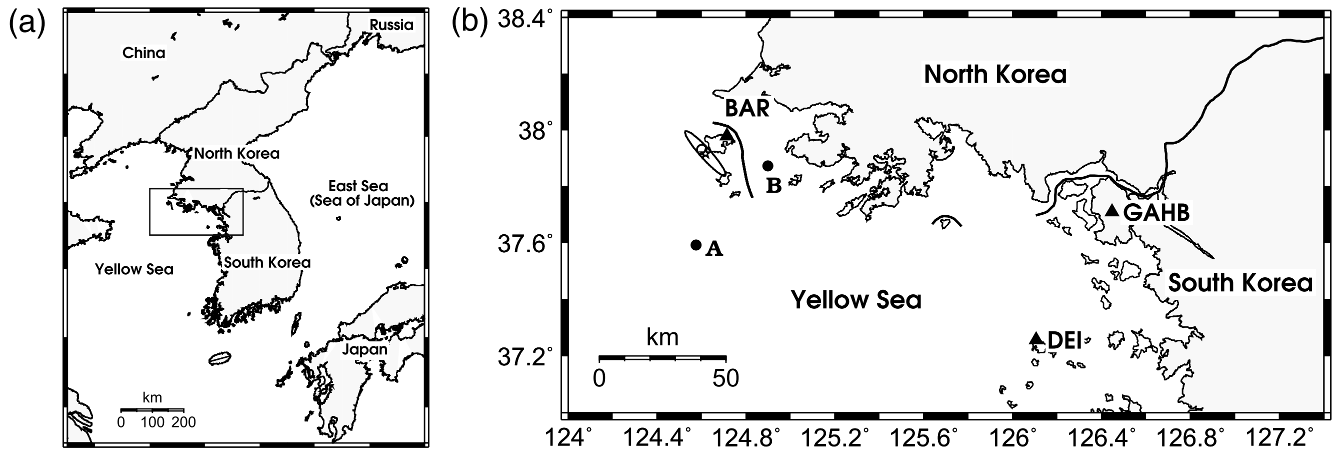

Figure 1. Map of the reported vessel-sinking location (open circle) and stations (triangles): (a) map of the Korean Peninsula and (b) an enlarged map around the sinking region. The area in (b) is marked with a rectangle in (a). Seismic records are collected from three local stations (BAR, DEI, GAHB). The event location determined from *P* and *S* arrival times is marked with a star inside the open circle. The 95% confidence ellipse of the determined event location is presented. The locations of two nearby earthquakes (A, B) are marked with closed circles. The national border between North Korea and South Korea is marked with solid lines.

natural earthquakes are dominated by shear waves, which is clearly different from the wave trains in Figure 2.

Methods

Polarization Analysis

P and *S* arrivals can be detected by polarization analysis, which is based on eigenvectors and eigenvalues of the covariance matrix of three-component seismograms. The horizontal polarization direction of an incident wave, ψ_h, can be calculated by (Vidale, 1986; Jurkevics, 1988)

$$\psi_h = \tan^{-1}\left[\frac{u_{e1}\,\mathrm{sign}(u_{z1})}{u_{n1}\,\mathrm{sign}(u_{z1})}\right], \quad (1)$$

where u_{i1} ($i = z, n, e$) is the direction cosine of the largest eigenvector, and parameter $\mathrm{sign}(u_{z1})$ accounts for the polarity of the seismic wave. The horizontal polarization direction indicates the horizontal incidence direction for a *P* wave, the 0°- or 180°-rotated direction for an *SV* wave, and the 90°- or 270°-rotated direction for an *SH* wave.

The vertical polarization direction, ψ_z, can be calculated by

$$\psi_z = \cos^{-1}|u_{z1}|. \quad (2)$$

The vertical incidence angle of a *P* wave is determined to be ψ_z, that of an *SV* wave is $90° - \psi_z$, and that of an *SH* wave is 90°. The rectilinearity of an incoming wave, χ_{rec}, is calculated by (Vidale, 1986; Jepsen and Kennett, 1990)

$$\chi_{\mathrm{rec}} = 1 - \frac{\lambda_2 + \lambda_3}{2\lambda_1}, \quad (3)$$

where λ_1, λ_2, and λ_3 are the eigenvalues in descending order (i.e., $\lambda_1 \geq \lambda_2 \geq \lambda_3$). The rectilinearity yields the degree of

Table 1
Event Information for the 26 March 2010 Sinking of the Korean Naval Vessel

Date (yyyy/mm/dd)	Time* (hh:mm:ss.s)	Latitude† (°N)	Longitude† (°E)	M_L†	$m_b(Pn)$‡	$m_b(Lg)$‡
2010/03/26	12:21:56.4	37.929	124.601	1.5	1.46(±0.26)	1.17(±0.20)

*Origin time refined in this study.
†Reported values (MCMJIG, 2010).
‡Body-wave magnitudes calculated in this study.

Table 2
Station Locations, *P* and *S* Arrival Times (t_p, t_s), and the Distances from Stations to the Reported Location of the Sinking of the Vessel

Station	Latitude (°N)	Longitude (°E)	Distance (km)	t_p (s)	t_s (s)
BAR	37.977	124.714	11.3	1.9	3.3
DEI	37.256	126.105	152.5	25.2	45.0
GAHB	37.708	126.447	164.4	26.9	47.8

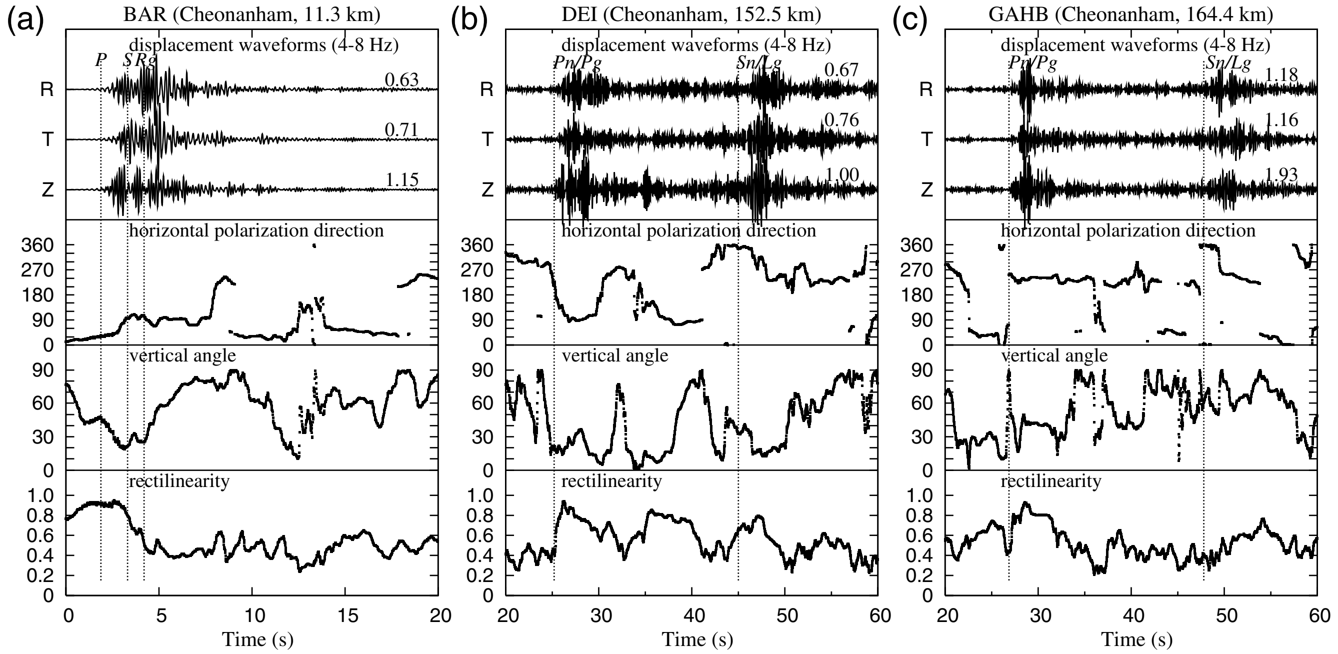

Figure 2. Seismic records of three stations and results of polarization analysis: stations (a) BAR, (b) DEI, and (c) GAHB. The waveform records are band-pass filtered between 4 and 8 Hz. The distances to stations are presented. Polarization analyses are applied to determine the arrival times of P and S waves. Horizontal and vertical polarization directions are determined, and the degrees of rectilinearity are measured. The arrival times of major phases are marked with dotted lines. The P/S amplitude ratios are annotated on seismograms.

polarization. The rectilinearity is typically high in direct phases, while it is low in reflected and/or scattered waves.

Magnitude Estimation

I measure body-wave magnitudes based on near-regional seismograms with high signal-to-noise ratios in high frequencies. I consider body-wave magnitude scales that are applicable to high-frequency signals. The $m_b(Lg)$ scale of Nuttli (1973) and the $m_b(Pn)$ scale of Evernden (1967) can be applied to events in the Korean Peninsula (Hong *et al.*, 2008). The $m_b(Pn)$ and $m_b(Lg)$ scales are given by

$$m_b(Pn) = -3.27 + 2\log\Delta + \log[A(Pn)/T(Pn)],$$
$$m_b(Lg) = -3.10 + 1.66\log\Delta + \log[A(Lg)/T(Lg)], \quad (4)$$

where Δ is the epicentral distance in kilometers, $A(Pn)$ is the zero-to-peak Pn displacement amplitude in nanometers, $A(Lg)$ is the peak-to-peak Lg displacement amplitude in nanometers, and $T(Pn)$ and $T(Lg)$ are the periods in seconds (Evernden, 1967; Nuttli, 1973; Herrmann and Nuttli, 1982; Hong *et al.*, 2008).

Location

The event location is estimated from P and S arrival times at multiple stations using a location method based on a 1D velocity model (Klein, 2007). I apply the 1D crustal model of Chang and Baag (2006).

The event location is additionally constrained using low-frequency horizontal waveforms of a single local station. The low-frequency seismograms of a local station are dominated by Rayleigh waves, which are polarized in the radial direction. The polarization direction of the Rayleigh waves can be found by searching the azimuthal direction in which the energy ratio between radial and tangential components is the largest.

When an arrival-time difference between P and S waves is given, the distance from the station to event can be calculated. From the estimated azimuth and distance, I can determine the event location.

Event Location and Confirmation

I pick the arrival times of P and S waves from the seismograms band-pass filtered between 4 and 8 Hz considering

Table 3
Two Earthquakes That Occurred near the Location of the Sinking of the Vessel

Event	Date (yyyy/mm/dd)	Time (hh:mm:ss.s)	Latitude (°N)	Longitude (°E)	Depth (km)	M_L
Event A	2009/08/25	14:08:27.4	37.591	124.575	8.0	3.0
Event B	2009/12/26	01:55:50.6	37.871	124.898	0.6	2.2

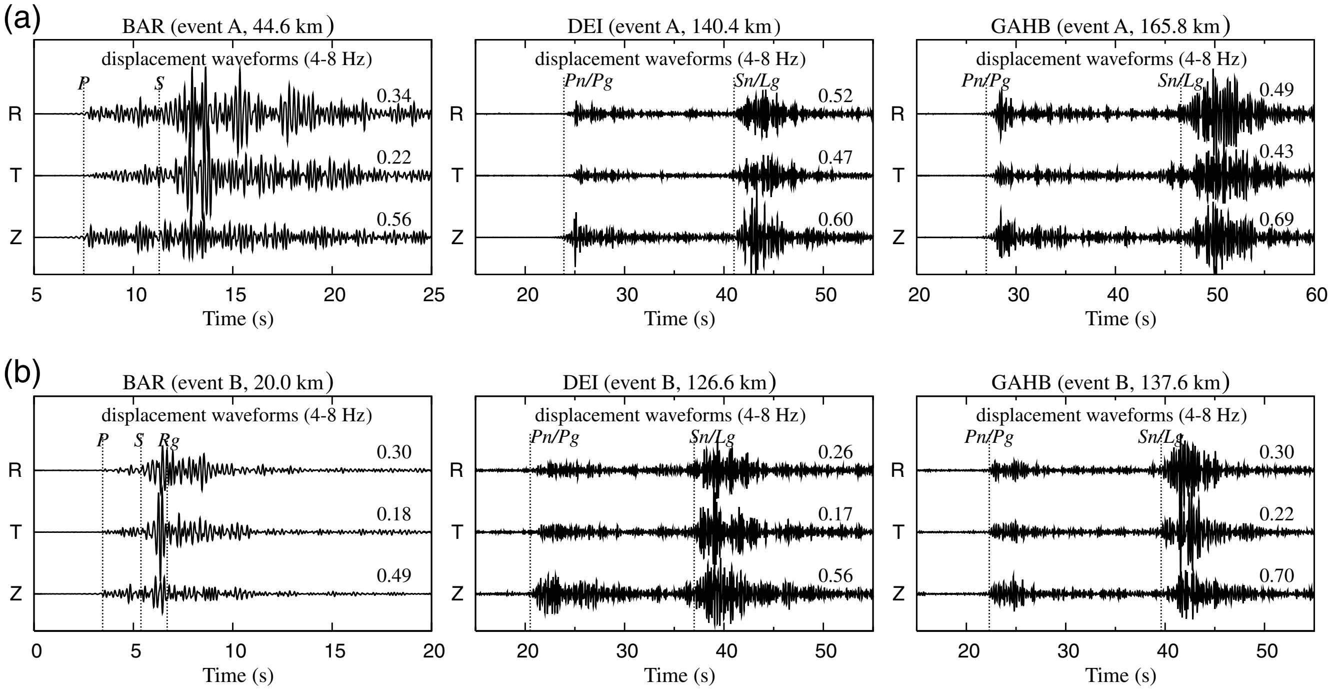

Figure 3. Displacement waveform records at stations BAR, DEI, and GAHB for two nearby earthquakes: (a) event A and (b) event B. The waveform records are band-pass filtered between 4 and 8 Hz. The distances to stations are presented. The arrival times of major phases are marked with dotted lines. The P/S amplitude ratios are annotated on seismograms. The P/S amplitude ratios are much smaller than those observed in Figure 2.

the variation of polarization and rectilinearity along wave trains (Fig. 2). The high-frequency scattered waves develop strongly in local and near-regional distances due to interference by small-scale heterogeneities that are distributed abundantly in the crust. The high-frequency records show complicated polarization and rectilinearity features. However, the horizontal polarization directions are determined to be the same or 180° different between P and S waves at the three stations. The vertical polarization angles are low for P phases, while they are similar or larger for S phases. The rectilinearity rates are high at P and S phases. Composite comparisons of polarization and rectilinearity features enable me to determine the arrival times of P and S waves.

The origin time of event is refined using the arrival-time difference between P and S waves considering a crustal velocity model (Chang and Baag, 2006). The event origin time is determined to be 12:21:56.4 UTC (Table 1), which agrees with the reported incident time (MCMJIG, 2010). Also, the event location is determined to be (37.915° N, 124.617° E) and a focal depth to be 0 km from the P and S arrival times. Here, the root mean square (rms) travel-time residual in the hypocenter inversion is given by 0.1 s. The estimated event location is ~2.1 km away in a southeast direction from the reported sinking location that is well confined in the 95% confidence ellipse (Fig. 1b). The accurate focal depth may be difficult to be resolved considering the rms travel-time residual and uncertainty in velocity model. However, the determined focal depth at least reflects a shallow depth close to the free surface.

I now estimate the event location from single-station records. The P and S travel times at station BAR are 1.9 s and 3.3 s, respectively (Table 2). I determine the distance from station BAR to the event considering the seismic velocities in the crust. The average P and S velocities in the crust are $\alpha = 5.6$–6.0 km/s and $\beta = 3.2$–3.6 km/s (Kennett *et al.*, 1995; Chang and Baag, 2006). The P–S arrival-time difference at station BAR is 1.4 s, corresponding to a distance range of 9.6–14.1 km considering the P and S velocities.

The back azimuth to the event is determined from analysis of low-frequency horizontal waveforms of station BAR. I analyze horizontal waveforms band-pass filtered between 1.0 and 1.4 Hz in which Rayleigh waves are dominant over body waves (Fig. 4a). The use of low-frequency waves allows me to analyze mainly the Rayleigh waves. I find that body waves are dominant at frequencies greater than 2.5 Hz. The horizontal polarization direction of the Rayleigh waves corresponds to the great-circle direction between source and receiver.

The horizontal polarization direction of the low-frequency waves is estimated by searching the back azimuths yielding the largest amplitude ratio between radial and tangential waveforms. Seismic records in a time window bounded by group velocities of $4.0 - 0.7$ km/s are analyzed (Fig. 4a). The amplitude ratios between radial and tangential waveforms as function of back azimuth are presented in Figure 4b. The largest radial amplitudes are found at 48° and 228°.

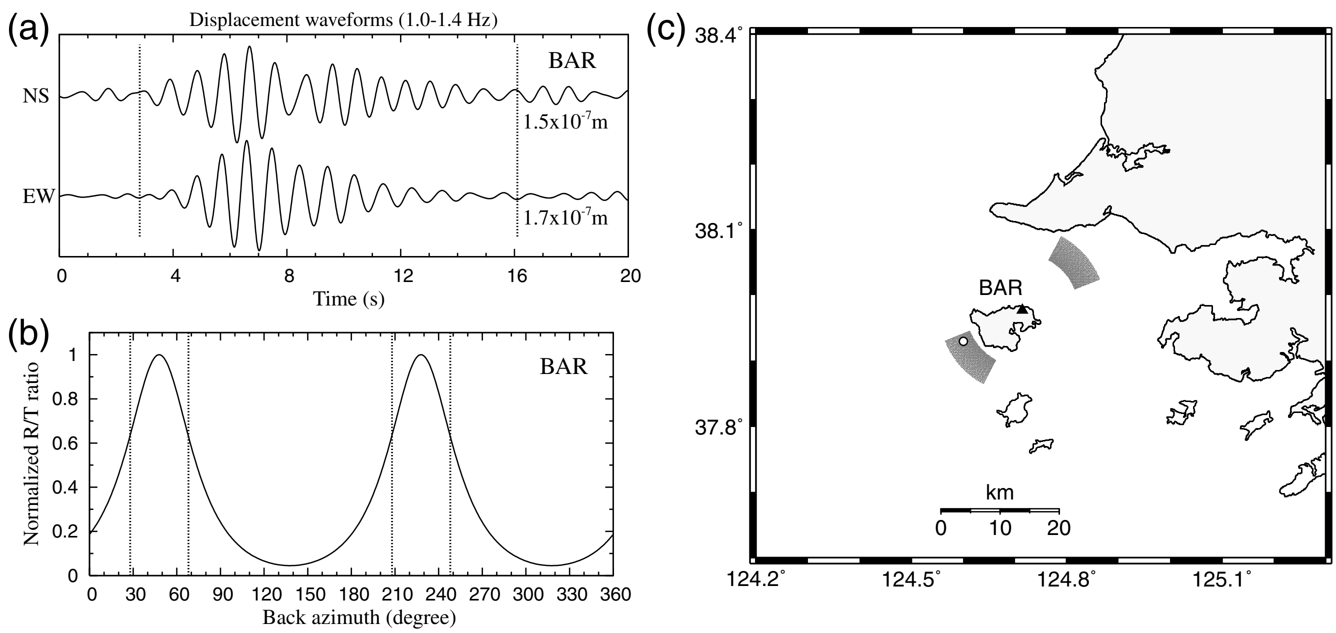

Figure 4. Determination of source region based on horizontal waveforms of station BAR. (a) Horizontal displacement waveforms bandpass filtered between 1.0 and 1.4 Hz; maximum amplitudes are presented. Solid lines, waveforms bounded by group velocities of 4.0–0.7 km/s. (b) Normalized amplitude ratios between radial and tangential components as a function of back azimuth. The amplitude ratios are periodic by 180°. The maximum amplitude ratio is observed at the azimuths of 48° and 228°. The angles of ±20° from the back azimuths with the maximum amplitude ratio are marked with solid lines. (c) The inferred source region is marked in gray. The source region is determined based on the *P–S* arrival-time difference and horizontal polarization direction. The reported sinking location is marked with a circle that lies on the inferred source region.

Seismic anisotropy in the crust may cause the Rayleigh waves to propagate in a path deviated from the great-circle direction. Considering the influence of seismic anisotropy, the actual great-circle direction is assumed to be found in angles of ±20° from the back azimuths with the largest amplitude ratio. Plausible source regions are determined based on the calculated distances and back azimuths (Fig. 4c). The reported sinking location lies within the inferred source region. The coincidence of the determined and reported event locations suggests that the observed seismograms are associated with the vessel-sinking.

Magnitude

The body-wave magnitudes are estimated from the near-regional records at stations DEI and GAHB for frequencies of 3–10 Hz in which seismic signals are dominant over background noise (Fig. 5). The *Pn* body-wave magnitude is larger than the *Lg* body-wave magnitude. The magnitudes are determined similarly among different stations. The average $m_b(Pn)$ is determined to be 1.48 with standard deviation of 0.23. The average $m_b(Lg)$ is determined to be 1.18 and the standard deviation is 0.17. The $m_b(Pn)$ estimate is close to the reported M_L.

Waveform Features

Station BAR is located at a distance of 11.3 km from the source. The direct *P* and *S* waves and their coda waves are well observed (Fig. 2). Stations DEI and GAHB are located at near-regional distances of 152.5 and 164.4 km, in which major *P* phases (*Pn*, *Pg*) have similar travel times. Also, the *Sn* and *Lg* have similar travel times. I observe comparable strengths of *P* and *S* phases. Note that *P* wave trains are

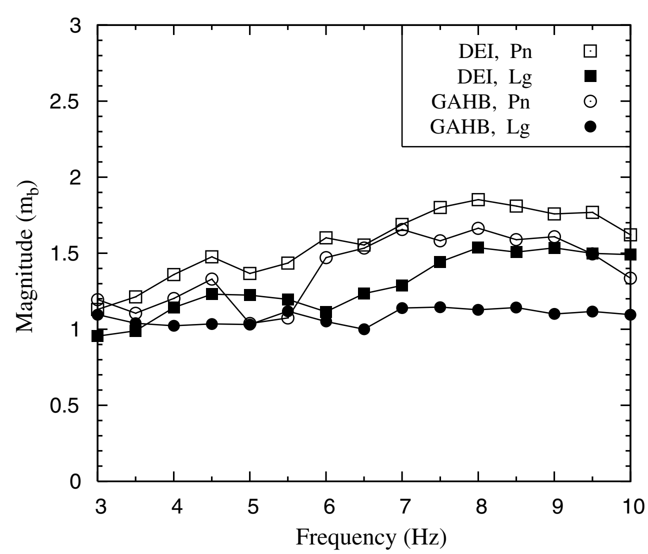

Figure 5. Body-wave magnitudes (m_b) based on *Pn* and *Lg* waves as functions of frequency between 3 and 10 Hz. Seismic waveforms at near-regional stations DEI and GAHB are analyzed. The $m_b(Pn)$ estimates are determined to be 1.3–1.7, and the $m_b(Lg)$ estimates are 1.0–1.5.

typically dominated by Pg waves, and S wave trains are dominated by Lg waves at near-regional or larger distances. The *P/S* amplitude ratios are determined to be 1.15–1.93 in vertical components, 0.63–1.18 in radial components, and 0.71–1.16 in tangential components (Fig. 2).

For comparison, the *P/S* amplitude ratios of two nearby natural earthquakes are determined to be 0.49–0.70 in vertical components, 0.26–0.52 in radial components, and 0.18–0.47 in tangential components (Fig. 3). I find that the *P/S* amplitude ratios of the earthquakes are much smaller than those of seismic waves originated from the vessel-sinking region. Note that underwater sources excite only the compressional waves, while faultings in solid media generate significant shear waves. Thus, shear waves are typically observed to be stronger than compressional waves in natural earthquakes, yielding low P/S amplitude ratios.

I theoretically examine *P*- and *S*-wave amplitudes for an underwater explosive source. I consider a simplified crustal model where oceanic and crustal layers are laid over a mantle half-space (Fig. 6a). The *P*- and *S*-wave velocities and the density in the oceanic layer are set to be 1.5 km/s, 0 km/s, and 1 g/cm^3 (Table 4). The seismic velocities and density (ρ_2) in the crust are set to be 6.3 km/s, 3.5 km/s, and 2.58 g/cm^3, considering the average seismic properties in the crust (Chang and Baag, 2006). The seismic velocities and the density of the mantle are set to be 7.95 km/s, 4.41 km/s, and 3.30 g/cm^3 (Chang and Baag, 2006; Hong and Kang, 2009).

An explosion source is implemented in the oceanic medium. Only *P* energy is excited from the source in the oceanic medium. *P* waves and wavetype-coupled *S* waves develop on the ocean-crust interface when the *P* energy in the oceanic medium transmits to the crust. Seismic waves observed in regional distances are transmitted through the crust and the Moho. Mantle-lid waves (*Pn*, *Sn*) develop when the waves are critically refracted on the Moho. Crustal-reflection waves (*Pg*, *Lg*) develop when waves are reflected on the Moho.

I calculate the amplitudes of *P* and *S* waves on the Moho to understand the amplitude variation of regional phases. The geometrical-spreading-effect-corrected seismic amplitudes at a certain interface can be calculated by multiplying the transmission coefficients on all interfaces between the source and the target interface.

When an isotropic unit impulse is excited in the oceanic medium, the geometrical-spreading-effect-corrected amplitudes of waves can be calculated by combining the transmission or reflection coefficients for the boundaries along the ray path. Thus, the transmitted (or reflected) *P*- and *S*-wave amplitude on the Moho can be calculated by

$$A_P^T = T_{PP}^1 \cdot T_{PP}^2, \qquad A_P^R = T_{PP}^1 \cdot R_{PP}^2,$$
$$A_S^T = T_{PS}^1 \cdot T_{SS}^2, \qquad A_S^R = T_{PS}^1 \cdot R_{SS}^2, \tag{5}$$

where A_i^T (or A_i^R) is the amplitude of refracted (or reflected) i phase on the Moho, and T_{ij}^1 is the i-to-i phase transmission

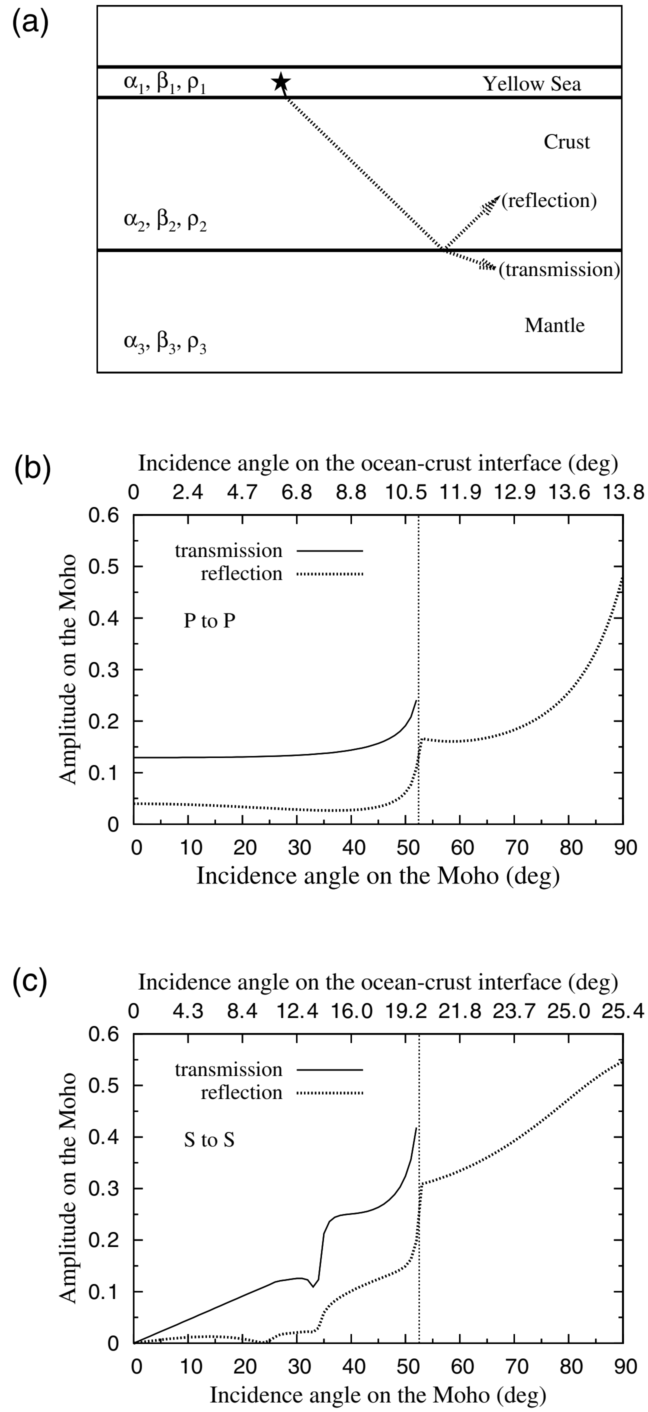

Figure 6. A simplified crustal model and reflection and transmission coefficients on the Moho: (a) model, (b) case of *P*-to-*P*, and (c) case of *S*-to-*S*. An explosion source is considered in the oceanic layer where only the *P* wave is excited. The reflection and transmission coefficients are presented as functions of incidence angle on the Moho. The corresponding incidence angles on the ocean-crust interface are also presented. The *S* waves develop from wavetype-coupling of *P* on the ocean-crust interface. The critically refracted *P* and *S* waves on the Moho develop as *Pn* and *Sn*. Waves reflected on the Moho are developed into *Pg* and *Lg*. The amplitudes of critically refracted *P* and *S* waves are comparable. Also, the amplitudes of post-critically reflected *P* and *S* waves are comparable.

Table 4
A Simplified Velocity Model for the Source Region*

Layer	α (km/s)	β (km/s)	ρ (g/cm^3)	h (km)
Layer 1 (Yellow Sea)	1.50	0	1.00	0.044
Layer 2 (Crust)	6.30	3.50	2.58	32
Layer 3 (Mantle)	7.95	4.41	3.30	–

*P and S wave velocities (α, β), densities ρ, and thicknesses (h) are presented.

coefficient on the ocean-crust interface. Also, T_{ij}^2 (or R_{ij}^2) is the i-to-j phase transmission (or reflection) coefficient between the crust and the mantle. The transmission and reflection coefficients are presented in Aki and Richards (2002, p. 144).

I consider the velocity model in Table 4. The geometrical-spreading-effect corrected seismic amplitudes on the Moho are calculated as function of incidence angle on the ocean-crust interface and its corresponding incidence angle on the Moho (Fig. 6b,c). Note that the incidence angles on the Moho are determined according to the incidence angle on the ocean-crust interface under the Snell's law. Because a unit impulse is considered in equation (5), the amplitudes reflect relative strengths compared with the original P amplitude in the oceanic medium.

The angle for P to P critical refraction on the Moho is 52.4°, which can be achieved when P energy is incident to the ocean-crust interface with an angle of 10.9° (Fig. 6b). Similarly, the angle for S to S critical refraction on the Moho is 52.6°, which can be achieved by P-to-S transmission across the ocean-crust interface with an incidence angle of 19.9° in the oceanic medium (Fig. 6c).

The amplitude of the critically refracted P wave on the Moho is determined to be ~0.24. That is, the geometrical-spreading-effect corrected Pn amplitude on the Moho is 0.24 times the original P amplitude in the oceanic medium (Fig. 6b). The largest amplitude of post-critically reflected P waves is about 0.48 times the original P amplitude. I find that the amplitudes of post-critically reflected P waves are larger than those of the pre-critically reflected P waves.

Similarly, the amplitudes of refracted and reflected S waves increase abruptly around the critical angle (Fig. 6c). The amplitudes of post-critically reflected S waves increase with incidence angle. The Sn amplitude on the Moho is about 0.42 times the original P amplitude. The largest amplitude of post-critically reflected S waves is about 0.55 times the original P amplitude. I find that the amplitudes of critically refracted P and S are comparable. A similar feature is observed between post-critically refracted P and S waves (Fig. 6b,c).

The Pn and Sn waves have similar ray paths to a station and experience similar geometrical spreading effects. A similar relationship is found between post-critically reflected P and S waves. The ratio between maximum P and S amplitudes is given to be ~0.87, which is close to the P/S ratios observed in the collected seismograms (Fig. 2). These observations are consistent with the features observed from underwater explosions.

Spectral Features and Source Strength

I now investigate the spectral contents of waves originated from the vessel-sinking. I analyze the P wave train at station BAR. The spectral amplitudes of P waves in the vertical-component displacement seismogram are measured in the time range of 1.71–2.69 s using a 1.3-s moving time window with 0.1-s-long cosine tapers (Fig. 7). The P energy is dominant over the background noise in the frequencies of 2–40 Hz. The P energy displays three peaks around 8.5, 17.7, and 34.6 Hz (p1, p2, p4 in Fig. 7).

The spectral peaks are a harmonic series that develop due to reverberation of compressional energy in the water column of the source region. This phenomenon is typically observed in seismic signals from underwater explosions (Weinstein, 1968; Bowers and Selby, 2009). The frequencies of the peaks correspond to multiples of the fundamental frequency, $f_0 \approx 8.5$ Hz.

The fundamental frequency (f_0) reflects the water-column thickness in the source region (Weinstein, 1968):

$$f_0 = \frac{c}{4h}, \tag{6}$$

where c is the wave speed in the water, and h is the thickness of water medium. When the wave speed in the water is set to be 1.5 km/s, the water-column thickness (h) is determined to be 44 m. The estimated water-column thickness agrees with the reported thickness, 47 m (MCMJIG, 2010). The spectral amplitude peaks are modulated following the depth of detonation (Bowers and Selby, 2009). I find relative suppression of the spectral peak around 26 Hz (p3 in Fig. 7), which reflects interference of multiply-reflected waves in the oceanic layer.

Acoustic Waves

The coda waves following the S waves last for several tens of seconds. I observe a high-frequency monotonic wave at 31.9 s after the P arrival in record sections band-pass filtered between 30 and 40 Hz (Fig. 8). The later high-frequency waves are stronger in the horizontal components than in the vertical component. The travel time of the wave is 33.8 s, corresponding to an apparent group velocity of ~335 m/s. The energy peaks at frequencies of ~32 Hz (Fig. 7). This energy corresponds to acoustic waves, which may develop from an explosive source or supersonic motion in the air or in a location close to the air (e.g., Kanamori *et al.*, 1991; Ichinose *et al.*, 1999; Koper *et al.*, 1999; Stump *et al.*, 2004; Gibbons *et al.*, 2007).

The acoustic-wave speed depends on the detonation strength, distance, atmospheric pressure, and temperature (Kinney and Graham, 1985; Koper *et al.*, 2002; Negraru *et al.*, 2010). The observed average speed is consistent with

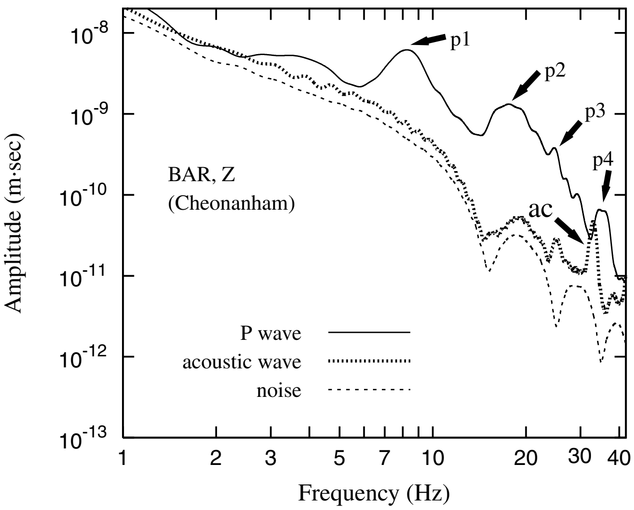

Figure 7. Spectral amplitudes of *P*, acoustic wave, and background noise in the vertical displacement seismogram at station BAR. The spectra of *P* and acoustic waves are calculated from waveforms in the lapse times of 1.71–2.69 s and 33.84–35.15 s. The level of background noise is estimated from a 2-s-long seismic record before *P* arrival. A 1.3-s-long moving time window with 0.1-s-long cosine tapers is applied to determine the average spectra. *P* waves are dominant over background noise in the frequencies greater than 2 Hz. Acoustic waves are strong at frequencies around 32 Hz (ac). Prominent spectral peaks (p1, p2, p4) are observed in the *P*-wave spectra at frequencies of 8.5 Hz and its multiples (17.7, 34.6 Hz). Modulation of spectral amplitudes at frequencies around 26 Hz (p3) is observed.

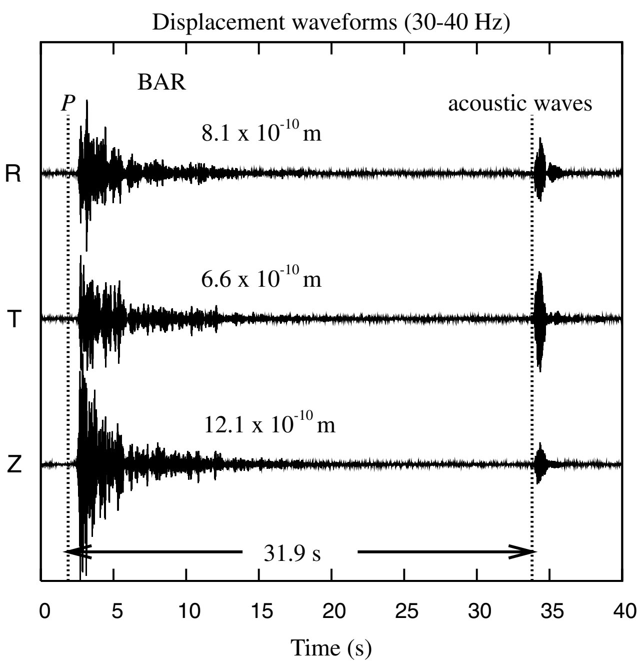

Figure 8. Three-component displacement waveforms of station BAR band-pass filtered between 30 and 40 Hz. Acoustic waves are observed in 31.9 s after the *P* arrival. The maximum amplitudes are annotated. The acoustic waves in the horizontal components are stronger than those in the vertical component.

previous observations (e.g., Koper *et al.*, 1999, 2002). In addition, the observation of stronger high-frequency energy in horizontal components is consistent with previous studies (e.g., Koper *et al.*, 1999).

The observation of acoustic wave suggests that the source is explosive, and the source depth is shallow. The identification of acoustic wave agrees with a testimony that a loud sound was heard at the time of vessel-sinking (MCMJIG, 2010). The travel time of the acoustic wave provides an additional constraint to the source location.

Discussion and Conclusions

I investigated local and near-regional seismic records at the time of the 26 March 2010 Korean naval vessel-sinking. The observed seismic records were confirmed to be associated with the Korean naval vessel-sinking from the determined event location and time. The determined event location agrees with the reported sinking location. The event origin time was refined from *P* and *S* arrival times. The body-wave magnitude based on *Pn* is determined to be 1.46, which is consistent with the reported M_L.

A high-frequency monotonic acoustic wave with an apparent group velocity of 335 m/s is observed. The acoustic-wave amplitudes in horizontal components are stronger than those in the vertical component, which is consistent with previous observations of acoustic waves. The travel time of the acoustic wave additionally constrains the event location. The observation of acoustic waves and high *P/S* amplitude ratios suggests an underwater explosion.

I also observed prominent peaks in *P*-wave spectra at frequencies of 8.5 Hz and its multiples, which corresponds to a harmonic series developing due to reverberation of compressional energy in the water column. The fundamental frequency reflects the thickness of the water column in the source region. The water-column thickness is determined to be 44 m, which is close to the reported thickness. Also, I observe modulation of spectral peaks that developed due to interference between multiply-reflected waves in the oceanic layer.

Data and Resources

Seismic waveform data were collected from the Korea Meteorological Administration (KMA) with permission.

Acknowledgments

I am grateful to the Korea Meteorological Administration (KMA) for making seismic data available. I thank Eunyoung Jo for assistance in calculating the event location. The paper benefitted from comments of Anton Dainty and two anonymous reviewers. This work was supported by the Korea Meteorological Administration Research and Development Program under Grant CATER 2007-5111.

References

Aki, K., and P. G. Richards (2002). *Quantitative Seismology*, Second Ed., University Science Books, Sausalito, California.

Baumgardt, D. R., and Z. Der (1998). Identification of presumed shallow underwater chemical explosions using land-based regional arrays, *Bull. Seismol. Soc. Am.* **88,** no. 2, 581–595.

Bowers, D., and N. D. Selby (2009). Forensic seismology and the comprehensive nuclear-test-ban treaty, *Annu. Rev. Earth Planet. Sci.* **37,** 209–236.

Chang, S.-J., and C.-E. Baag (2006). Crustal structure in southern Korea from joint analysis of regional broadband waveforms and travel times, *Bull. Seismol. Soc. Am.* **96,** 856–870.

Evernden, J. F. (1967). Magnitude deterimination at regional and near-regional distances in the United States, *Bull. Seismol. Soc. Am.* **57,** 591–639.

Evers, L. G., L. Ceranna, H. W. Haak, A. Le Pichon, and R. W. Whitaker (2007). A seismoacoustic analysis of the gas-pipeline explosion near Ghislenghien in Belgium, *Bull. Seismol. Soc. Am.* **97,** 417–425.

Gibbons, S. J., F. Ringdal, and T. Kværna (2007). Joint seismic-infrasonic processing of recordings from a repeating source of atmospheric explosions, *J. Acoust. Soc. Am.* **122,** no. 5, EL158–EL164.

Herrmann, R. B., and O. W. Nuttli (1982). Magnitude: The relation of M_L to m_{bLg}, *Bull. Seismol. Soc. Am.* **72,** 389–397.

Hong, T.-K., and T.-S. Kang (2009). *Pn* travel-time tomography of the paleo-continental-collision and rifting zone around Korea and Japan, *Bull. Seismol. Soc. Am.* **99,** no. 1, 416–421.

Hong, T.-K., C.-E. Baag, H. Choi, and D.-H. Sheen (2008). Regional seismic observations of the October 9, 2006 underground nuclear explosion in North Korea and the influence of crustal structure on regional phases, *J. Geophys. Res.* **113,** B03305, doi 10.1029/2007JB004950.

Ichinose, G. A., K. D. Smith, and J. D. Anderson (1999). Seismic analysis of the 7 January 1998 chemical plant explosion at Kean Canyon, Nevada, *Bull. Seismol. Soc. Am.* **89,** no. 4, 938–945.

Jepsen, D. C., and B. L. N. Kennett (1990). Three-component analysis of regional seismograms, *Bull. Seismol. Soc. Am.* **80,** 2032–2052.

Jurkevics, A. (1988). Polarization analysis of three-component array data, *Bull. Seismol. Soc. Am.* **78,** 1725–1743.

Kanamori, H., J. Mori, D. L. Anderson, and T. H. Heaton (1991). Seismic excitation by the space shuttle Columbia, *Nature* **349,** 781–782.

Kennett, B. L. N., E. R. Engdahl, and R. Buland (1995). Constraints on seismic velocities in the earth from travel times, *Geophys. J. Int.* **122,** 108–124.

Kim, W.-Y., L. R. Sykes, J. H. Armitage, J. K. Xie, K. H. Jacob, P. G. Richards, M. West, F. Waldhauser, J. Armbruster, L. Seeber, W. X. Du, and A. Lerner-Lam (2001). Seismic waves generated by aircraft impacts and building collapses at World Trade Center, New York City, *Eos Trans. AGU*, American Geophysical Union, **82,** no. 47, 565, 570–571.

Kinney, G. F., and K. J. Graham (1985). *Explosive Shocks in Air*, Second Ed., Springer-Verlag, New York.

Klein, F. W. (2007). User's Guide to HYPOINVERSE-2000, a Fortran program to solve for earthquake locations and magnitudes, *U.S. Geol. Surv. Open-File Rept. 02-171*, revised, Version 1.1.

Koper, K. D., T. C. Wallace, and D. Hollnack (1999). Seismic analysis of the 7 August 1998 truck-bomb blast at the American embassy in Nairobi, Kenya, *Seismol. Res. Lett.* **70,** no. 5, 512–521.

Koper, K. D., T. C. Wallace, R. E. Reinke, and J. A. Leverette (2002). Empirical scaling laws for truck bomb explosions based on seismic and acoustic data, *Bull. Seismol. Soc. Am.* **92,** no. 2, 527–542.

Koper, K. D., T. C. Wallace, and R. C. Aster (2003). Seismic recordings of the Carlsbad, New Mexico, pipeline explosion of 19 August 2000, *Bull. Seismol. Soc. Am.* **93,** no. 4, 1427–1432.

Multinational Civilian-Military Joint Investigation Group (MCMJIG) (2010). *Joint Investigation Report: On the Attack Against ROK Ship Cheonan*, Ministry of National Defense, Republic of Korea, 313 pp.

Negraru, P. T., P. Golden, and E. T. Herrin (2010). Infrasound propagation in the "Zone of Silence", *Seismol. Res. Lett.* **81,** no. 4, 614–624.

Nuttli, O. W. (1973). Seismic wave attenuation and magnitude relations for eastern North America, *J. Geophys. Res.* **78,** 876–885.

Plutchok, R., and P. Broome (1969). Modeling of seismic signals from large underwater explosions to predict the spectra and covariance functions, *Bull. Seismol. Soc. Am.* **59,** no. 3, 1137–1147.

Stump, B., M.-S. Jun, C. Hayward, J.-S. Jeon, I.-Y. Che, K. Thomason, S. M. House, and J. McKenna (2004). Small-aperture seismo-acoustic arrays: Design, implementation, and utilization, *Bull. Seismol. Soc. Am.* **94,** no. 1, 220–236.

Vidale, J. E. (1986). Complex polarization analysis of particle motion, *Bull. Seismol. Soc. Am.* **76,** no. 5, 1393–1405.

Weinstein, M. S. (1968). Spectra of acoustic and seismic signals generated by underwater explosions during Chase experiment, *J. Geophys. Res.* **73,** no. 16, 5473–5476.

Yonsei University
Department of Earth System Sciences
Shinchon-dong, 134
Seodaemun-gu, Seoul 120-749
South Korea
tkhong@yonsei.ac.kr

Manuscript received 1 July 2010